

A Theory for the Hadley Cell Descending and Ascending Edges throughout the Annual Cycle

SPENCER A. HILL,^{a,b} SIMONA BORDONI,^{c,d} AND JONATHAN L. MITCHELL^{e,f}

^a Program in Atmospheric and Oceanic Sciences, Princeton University, Princeton, New Jersey

^b Lamont-Doherty Earth Observatory, Columbia University, Palisades, New York

^c Department of Civil, Environmental and Mechanical Engineering (DICAM), University of Trento, Trento, Italy

^d Division of Geological and Planetary Sciences, California Institute of Technology, Pasadena, California

^e Department of Atmospheric and Oceanic Sciences, University of California, Los Angeles, Los Angeles, California

^f Department of Earth, Planetary, and Space Sciences, University of California, Los Angeles, Los Angeles, California

(Manuscript received 27 December 2021, in final form 28 June 2022)

ABSTRACT: We present a theory for the latitudinal extents of both Hadley cells throughout the annual cycle by combining our recent scaling for the ascending edge latitude based on low-latitude supercriticality with the theory for the poleward, descending edge latitudes of Kang and Lu based on baroclinic instability and a uniform Rossby number (Ro) within each cell's upper branch. The resulting expressions for all three Hadley cell edges are predictive except for diagnosed values of Ro and two proportionality constants. Thermal inertia—which damps and lags the ascent latitude relative to the insolation—is accounted for semianalytically through the Mitchell et al. model of an “effective” seasonal forcing cycle. Our theory, given empirically an additional ~ 1 -month lag for the descending edge, captures the climatological annual cycle of the ascending and descending edges in an Earthlike simulation in an idealized aquaplanet general circulation model (GCM). In simulations in this and two other idealized GCMs with varied planetary rotation rate (Ω), the winter, descending edge of the solstitial, cross-equatorial Hadley cell scales approximately as $\Omega^{-1/2}$ and the summer, ascending edge as $\Omega^{-2/3}$, both in accordance with our theory. Possible future refinements and tests of the theory are discussed.

KEYWORDS: Atmospheric circulation; Hadley circulation; Idealized models

1. Introduction

Climatologically over the annual cycle, the poleward, descending edges of the Hadley cells vary meridionally by $\lesssim 5^\circ$ latitude about their annual-mean positions, considerably less than the $\sim 15^\circ\text{S}$ – 15°N range of the shared, ascending edge (cf. Fig. 4 of Adam et al. 2016). These result in a pronounced seasonal cycle of zonal-mean rainfall in the deep tropics versus more consistently dry conditions in the subtropics. Regional hydrological deviations from the zonal average are pronounced—with, for example, intense Indian summer monsoon rainfall spanning roughly the same latitudes as the Sahara and Arabian Deserts (Rodwell and Hoskins 1996)—nevertheless, we focus on the zonal-mean dynamical problem, seeking a minimal explanation for the differing annual cycles of the Hadley cell descending and ascending edges (henceforth φ_d and φ_a , respectively, and formally defined below in terms of the mass overturning streamfunction).

For φ_d , our starting point is the theory of Kang and Lu (2012, henceforth KL12), whose own starting point is that of Held (2000, henceforth H00) for the annual-mean φ_d that assumes the Hadley cells terminate where their zonal wind profiles become baroclinically unstable. KL12 extend the H00 model in two key ways. First, they generalize from the annual mean to the annual cycle by accounting, albeit diagnostically, for off-equatorial φ_a . For angular-momentum-conserving (AMC) zonal winds as assumed by H00, ascent off the equator results in less positive zonal winds at each latitude (Lindzen and Hou 1988, hereafter LH88) and thus

to baroclinic instability onset occurring farther poleward than for equatorial ascent. All else equal, this would cause φ_d to be farther poleward in solstitial seasons when φ_a is farther off-equator than in equinoctial seasons. An example of this framework's utility is Hilgenbrink and Hartmann (2018), who interpret changes in φ_d throughout the annual cycle caused by ocean heat transports in terms of changes in φ_a .

Second, KL12 relax the H00 assumption of strictly AMC winds by assuming that the Rossby number (Ro) is uniform throughout each Hadley cell's upper branch but not necessarily unity. Its formal definition follows below, but for now Ro is exactly unity for AMC winds and exactly zero if zonal winds themselves are zero, and KL12 derive an analytical expression for the meridional profile of zonal wind under uniform $0 < Ro \leq 1$. In simulations (Walker and Schneider 2006) and reanalysis data (Schneider 2006), Ro is regularly below unity and typically smaller in the equinoctial and summer cells than in the cross-equatorial winter cell (Bordoni and Schneider 2008; Schneider and Bordoni 2008). By diagnosing a bulk value of Ro for each cell and meteorological season in addition to φ_a , KL12 provide closed expressions for the Northern and Southern Hemisphere descending edge latitudes in all four seasons.¹

¹ Other authors also have considered a uniform Ro in the tropical upper troposphere. Becker et al. (1997) find that a uniform $Ro = 0.5$ approximation [their Fig. 7 and Eq. (28)] adequately captures the vorticity distribution in the descending branch of the winter Hadley cell in their simplified, dry GCM. Zurita-Gotor and Held (2018) discuss the absolute vorticity distribution corresponding to uniform Ro .

Corresponding author: Spencer Hill, spencerh@princeton.edu

DOI: 10.1175/JAS-D-21-0328.1

© 2022 American Meteorological Society. For information regarding reuse of this content and general copyright information, consult the AMS Copyright Policy (www.ametsoc.org/PUBSReuseLicenses).

For φ_a , in Hill et al. (2021) we presented a scaling for φ_a by assuming that it is set by the meridional extent of supercritical radiative forcing in the summer hemisphere (the meaning of which we expand upon below). In essence, the present study simply replaces the diagnosed φ_a in the KL12 model with this predictive scaling. The one departure from Hill et al. (2021)—which implicitly treated thermal inertia as negligible by relating the seasonally varying φ_a to the contemporaneous insolation—is accounting for thermal inertia's damping and delaying of the φ_a annual cycle via the analytical model of Mitchell et al. (2014). The result is a unified theory for φ_a and both hemispheres' φ_d with only two proportionality constants as well as Ro diagnosed (potentially with distinct Ro values required for each cell and season).

Separately, in general circulation model (GCM) simulations with differing planetary rotation rates (Ω) the solstitial, cross-equatorial Hadley cell expands into both the summer and winter hemispheres as Ω decreases (e.g., Faulk et al. 2017; Singh 2019). But whereas in an Earthlike regime the summer φ_a and winter φ_d are comparably poleward, in slowly rotating cases the summer φ_a is farther poleward than the winter φ_d : the cross-equatorial Hadley cell becomes increasingly lopsided about the equator [e.g., Fig. 5 of Guendelman and Kaspi (2018) and Fig. 12 of Guendelman and Kaspi (2019)].² Moreover, Guendelman and Kaspi (2019) empirically find distinct best-fit power-law exponents for the two edges, close to $\varphi_a \propto \Omega^{-2/3}$ and $\varphi_d \propto \Omega^{-1/2}$. We will use our theory along with idealized GCM simulations to explain these exponents and how they relate to the lopsidedness of the cross-equatorial cell.

In the following sections we

- derive and describe fixed-Ro zonal wind, angular momentum, and depth-averaged potential temperature fields (section 2);
- present our unified theory, which essentially combines the KL12 model for φ_d with the Hill et al. (2021) theory for φ_a (section 3);
- and test our theory against idealized GCM simulations, first over the annual cycle in one moist model and second for the solstitial Hadley circulation across rotation rates in one dry and two moist models (section 4).

We then conclude with summary and discussion (section 5).

2. Uniform-Ro fields

In general, absolute angular momentum is

$$M = a \cos \varphi (\Omega a \cos \varphi + u), \quad (1)$$

where a is planetary radius, φ is latitude, and u is the zonally averaged zonal wind. This can be considered the sum of planetary angular momentum, $M_p(\varphi) \equiv \Omega a^2 \cos^2 \varphi$, and relative angular momentum $ua \cos \varphi$. The corresponding AMC zonal wind field—for which angular momentum is meridionally uniform

and equal to the planetary angular momentum value $M_p(\varphi_a)$ at a specified latitude φ_a —is

$$u_{\text{amc}}(\varphi) = \Omega a \cos \varphi \left(\frac{\cos^2 \varphi_a}{\cos^2 \varphi} - 1 \right). \quad (2)$$

For the Hadley cells, we equate φ_a in (2) with the cells' ascending edge on the grounds that ascent out of the viscous boundary layer there transmits the local planetary angular momentum $M_p(\varphi_a)$ to the comparatively inviscid free troposphere (Held and Hou 1980; LH88). This neglects the finite width of the ascent branch (Watt-Meyer and Frierson 2019; Byrne and Thomas 2019), but in principle one could compute an effective ascent latitude by averaging the planetary angular momentum over the full extent of the ascending branch, perhaps weighting by the vertical velocity out of the boundary layer at each latitude.

The Rossby number is defined as

$$\text{Ro} \equiv -\frac{\zeta}{f}, \quad (3)$$

where $\zeta \equiv -(a \cos \varphi)^{-1} \partial_\varphi (u \cos \varphi)$ is zonal-mean relative vorticity and $f \equiv 2\Omega \sin \varphi$ is the planetary vorticity (i.e., the Coriolis parameter). Absolute vorticity is given by $\eta = f + \zeta = f(1 - \text{Ro})$. Absolute vorticity is proportional to the meridional gradient of angular momentum, and as such in an AMC state necessarily $\eta = 0$ and $\text{Ro} = 1$. In discussing the GCM simulations below, we will make use of a generalized version of Ro (Singh 2019), but (3) is the quantity used in the fixed-Ro fields we now define.

From (3), $\zeta = -\text{Ro}f$. If $\text{Ro} < 1$ but horizontally uniform, integrating meridionally yields the fixed-Ro zonal wind field,

$$u_{\text{Ro}}(\varphi) = \text{Ro} u_{\text{amc}}(\varphi), \quad (4)$$

which is simply the AMC zonal wind field scaled by Ro .³ The corresponding angular momentum field is

$$M_{\text{Ro}}(\varphi) = \Omega a^2 [\text{Ro} \cos^2 \varphi_a + (1 - \text{Ro}) \cos^2 \varphi], \quad (5)$$

which is a Ro-weighted average of the planetary angular momentum at the ascent latitude, $M_p(\varphi_a)$, and the full meridional distribution of the planetary angular momentum, $M_p(\varphi)$.

Finally, though it does not enter into our model for the Hadley cell edges below, we present for a Boussinesq atmosphere [see, e.g., Eq. (1) of Hill et al. (2019) for the full underlying system of equations] the depth-averaged potential temperature field in gradient balance with u_{Ro} . Denoted $\hat{\theta}_{\text{Ro}}$, it is given by

$$\frac{\hat{\theta}_a - \hat{\theta}_{\text{Ro}}(\varphi)}{\hat{\theta}_0} = \frac{\text{Ro}}{2\text{Bu}} \left\{ (2 - \text{Ro}) \cos^2 \varphi + \cos^2 \varphi_a \right. \\ \left. \times \left[4(1 - \text{Ro}) \ln \left(\frac{\cos \varphi_a}{\cos \varphi} \right) + \text{Ro} \frac{\cos^2 \varphi_a}{\cos^2 \varphi} - 2 \right] \right\}, \quad (6)$$

² This strictly applies to nonaxisymmetric atmospheres. It does not emerge clearly in simulations of axisymmetric atmospheres, which on theoretical grounds should exhibit φ_d poleward of $-\varphi_a$ (Hill et al. 2019).

³ Davis and Birner (2022) present what amounts to (4) (i.e. u_{amc} multiplied by a less-than-unity constant) from heuristic grounds albeit without reference to Ro; it should be noted that they also challenge the physical validity of baroclinic instability onset determining Hadley cell extent.

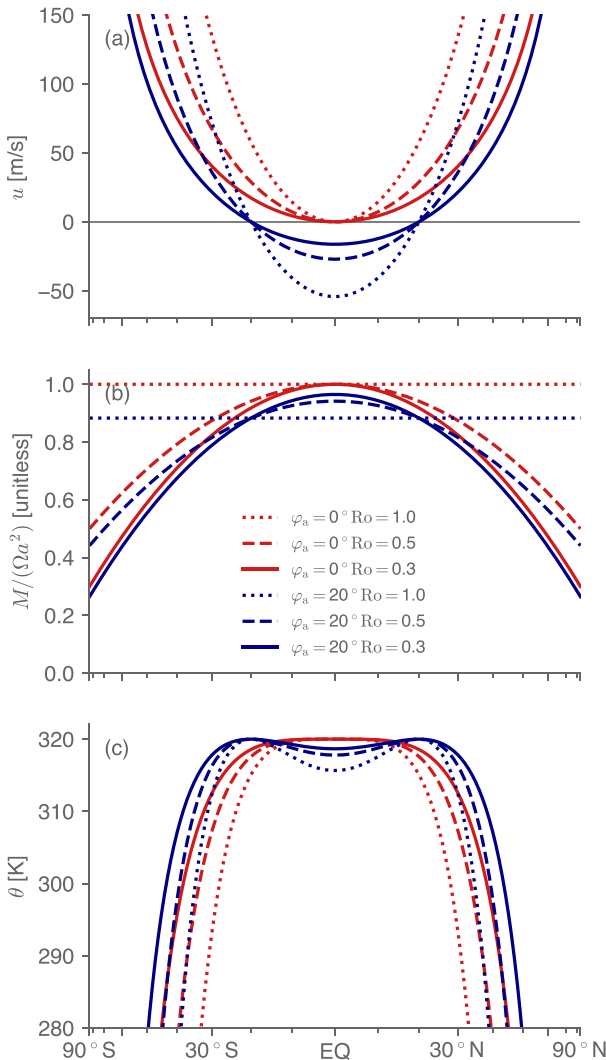


FIG. 1. Example (a) zonal wind (u_{Ro} , in $m\ s^{-1}$), (b) angular momentum (M_{Ro} , normalized by Ωa^2 and thus unitless), and (c) depth-averaged potential temperature ($\hat{\theta}_{Ro}$, in K) fields under a uniform Rossby number. Red curves are for $\varphi_a = 0$ and blue curves $\varphi_a = 20^\circ S/N$, while dotted, dashed, and solid curves are for $Ro = 1.0, 0.5,$ and 0.3 , respectively. Horizontal axis spacing is in $\sin \varphi$.

where $\hat{\theta}_a$ is the depth-averaged potential temperature at the latitude φ_a , θ_0 is the Boussinesq reference potential temperature,

$$Bu \equiv \frac{gH}{(\Omega a)^2} \tag{7}$$

is the planetary Burger number with gravity g and tropopause height H , and we have assumed that u_{Ro} occurs near the tropopause while $u \approx 0$ at the surface.

Figure 1 shows example u_{Ro} , M_{Ro} , and $\hat{\theta}_{Ro}$ fields with $Ro = 1, 0.5,$ or 0.3 and $\varphi_a = 0^\circ$ or 20° . For zonal wind, irrespective of Ro and φ_a , u_{Ro} vanishes at φ_a and increases monotonically moving away from the equator. If $\varphi_a \neq 0$, u_{Ro} is negative from $-\varphi_a$ to φ_a , minimizing at the equator. Both moving φ_a off

equator and decreasing Ro act to make the westerlies less positive. For example, at $30^\circ S/N$, $u_{Ro} \approx 133, 67,$ and $40\ m\ s^{-1}$, respectively, for $Ro = 1, 0.5,$ and 0.3 if $\varphi_a = 0$ or $71, 36,$ and $21\ m\ s^{-1}$, respectively, if $\varphi_a = 20^\circ$. For angular momentum, irrespective of Ro and φ_a , M_{Ro} at φ_a is equal to the local planetary angular momentum $M_p(\varphi_a)$; if $Ro = 1$, all latitudes take this value. For $Ro < 1$, it maximizes at the equator and decreases monotonically moving poleward. For the gradient-balanced potential temperature, $\hat{\theta}_{Ro}$ maximizes at φ_a irrespective of Ro and φ_a and for $\varphi_a \neq 0$ has a local minimum at the equator. As Ro increases, the meridional temperature gradients increase in magnitude, with a deeper equatorial dip and a more equatorward shoulder poleward of φ_a where temperatures begin dropping rapidly toward the pole.

3. Combined theory for Hadley cell ascending and descending edges

We now use these fixed- Ro fields to derive an expression for φ_d given values of Ro and φ_a that closely follows KL12. We then introduce within it our scaling for φ_a , yielding our unified theory for φ_d and φ_a . We then incorporate the influence of surface thermal inertia on the seasonal cycles of φ_a analytically and on φ_d more empirically.

a. Baroclinic instability onset theory for the Hadley cell edge with $Ro < 1$

Following H00, the baroclinic instability criterion for the two-layer model is approximately

$$\frac{u}{\Omega a} = Bu \Delta_\nu \frac{\cos \varphi}{\sin^2 \varphi}, \tag{8}$$

where u is the zonal wind in the upper layer, the wind in the lower layer has been assumed small enough to neglect, and Δ_ν is a static stability parameter representing the bulk fractional increase in potential temperature from the surface to the tropopause.^{4,5} H00 applies this to the annual-mean Hadley cells by assuming on-equatorial ascent, that the zonal winds are AMC, and that the descending edge is identical to this baroclinic instability onset latitude. Formally, taking $\varphi_a \approx 0$, using (2) for u in (8), and taking the small-angle limit yields the original H00 theory for φ_d , which we denote φ_{H00} :

$$\varphi_{H00} = (Bu \Delta_\nu)^{1/4}. \tag{9}$$

Using u_{Ro} (4) rather than u_{amc} (2) as the zonal-wind profile in (8), for $Ro < 1$ the predicted cell edge becomes

⁴ H00 uses the symbol R to denote the planetary Burger number, which elsewhere (Held and Hou 1980; Hill et al. 2019) is used for the thermal Rossby number. To prevent confusion, we use the more explicit notation Bu for the planetary Burger number and Ro_{th} for the thermal Rossby number.

⁵ The tropopause depth H , which for the H00 theory is strictly the local tropopause height, is assumed horizontally uniform and unmodified by the large-scale circulation from its forcing value corresponding to latitude-by-latitude radiative-convective equilibrium; see Hill et al. (2020) for justification.

$$\varphi_{\text{Ro,ann}} = \left(\frac{\text{Bu}\Delta_v}{\text{Ro}} \right)^{1/4} = \text{Ro}^{-1/4} \varphi_{\text{H00}}, \quad (10)$$

with φ_{H00} given by (9). This displaces the cell edge prediction poleward by, for example, $\sim 19\%$ if $\text{Ro} = 0.5$ or $\sim 50\%$ if $\text{Ro} = 0.2$. Using the original $H = 10$ km and $\Delta_v = 1/8$ parameter values from [Held and Hou \(1980\)](#) yields $\text{Bu} \approx 0.46$ and $\varphi_{\text{H00}} \approx 28^\circ$, which becomes approximately 33.3° if $\text{Ro} = 0.5$ or 41.9° if $\text{Ro} = 0.2$. This poleward displacement as Ro decreases coheres with physical intuition: because the upper-layer zonal wind magnitude at each latitude decreases as Ro decreases, the two-layer baroclinic instability onset criterion is met farther poleward.

For $\varphi_a \neq 0$, using (4) in (8) gives without approximation

$$\frac{\sin^4 \varphi_d}{\cos^2 \varphi_d} - \sin^2 \varphi_a \frac{\sin^2 \varphi_d}{\cos^2 \varphi_d} - \frac{\text{Bu}\Delta_v}{\text{Ro}} = 0, \quad (11)$$

where φ_d is the descending edge. From (10) the last term could equivalently be written $-\varphi_{\text{Ro,ann}}^4$. These arguments serve equally for the cross-equatorial, winter cell and the summer cell (provided it exists), depending on which cell the chosen Ro value is representative of. A corollary is that if the mean Ro value is the same in both cells, then the Hadley circulation extends equally far into either hemisphere irrespective of φ_a . Note that our assumption of uniform Ro throughout either cell differs slightly from [KL12](#), who assume $\text{Ro} = 1$ from the summer hemisphere edge of the cross-equatorial cell to the equator, a uniform $\text{Ro} \leq 1$ value in the winter hemisphere, and a uniform $\text{Ro} \leq 1$ value throughout the summer cell.

We have performed a 2D parameter sweep over φ_a and $(\text{Bu}\Delta_v/\text{Ro})^{1/4}$, from 0° to 90° in 1° increments for φ_a and from 0 to 2 in 0.01 increments for $(\text{Bu}\Delta_v/\text{Ro})^{1/4}$, solving (11) numerically for each pair of parameter values. The results are shown as shaded contours in [Fig. 2](#).⁶ Recalling that $\varphi_{\text{Ro,ann}} \equiv (\text{Bu}\Delta_v/\text{Ro})^{1/4}$, the right vertical axis shows the equivalent values of $\varphi_{\text{Ro,ann}}$ up to 90° , above which the small-angle solution obviously is nonsensical but the full solution retains its validity. The value of φ_d increases monotonically with φ_a and with $(\text{Bu}\Delta_v/\text{Ro})^{1/4}$. Close to the vertical axis of [Fig. 2](#), $|\varphi_{\text{Ro,ann}}/\varphi_a| \gg 1$, and $\varphi_d \approx \varphi_{\text{Ro,ann}}$: φ_a is negligibly off-equator. Close to the horizontal axis, $|\varphi_{\text{Ro,ann}}/\varphi_a| \ll 1$, and thus $\varphi_d \approx \varphi_a$. This regime usefully describes cases where the summer cell effectively disappears, as in all of the perpetual solstice simulations we will discuss below. For the winter hemisphere, the interpretation is that baroclinic instability onset occurs just poleward of $-\varphi_a$, near enough that it can be approximated as $-\varphi_a$. For intermediate values, if, e.g., $\varphi_a = \varphi_{\text{Ro,ann}}$, then φ_d is displaced 27% poleward of φ_a . We note that $|\varphi_d| \geq |\varphi_a|$; the descending edge latitude is always at or poleward of the ascending edge latitude. This is appropriate for the summer hemisphere φ_d but will prove imperfect for the winter φ_d in the idealized GCM simulations across rotation rates discussed below.

⁶ Over most of the parameter space, this quartic equation has only two solutions, which correspond to $\pm\varphi_d$. Two additional solutions straddling very close to zero can appear for sufficiently large φ_a but are not physically meaningful.

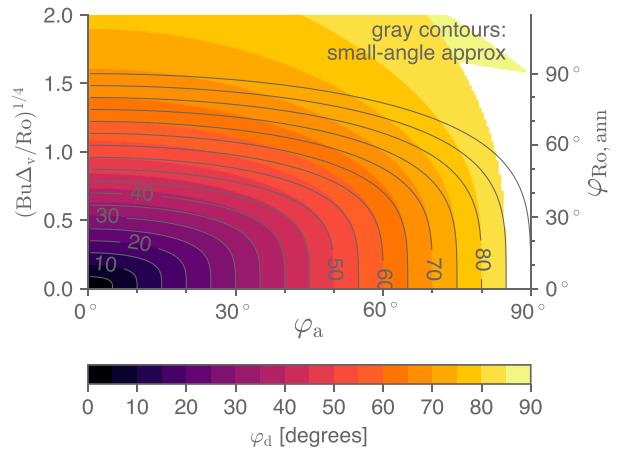


FIG. 2. Numerical solutions of (11) for values of φ_a and of $(\text{Bu}\Delta_v/\text{Ro})^{1/4}$, with φ_a sampled from 0° to 90° in 1° increments and $(\text{Bu}\Delta_v/\text{Ro})^{1/4}$ (which is dimensionless) from 0 to 2.0 in 0.01 increments. The right vertical axis labels are the $\varphi_{\text{Ro,ann}}$ solutions from 0° to 90° corresponding to the given $(\text{Bu}\Delta_v/\text{Ro})^{1/4}$ values. Areas in white indicate that the simple numerical algorithm used did not converge, but clearly they correspond to φ_d very near the pole. Contours are from 5° to 90° in 5° increments according to the color bar. Overlaid gray contours are the corresponding small-angle solutions obtained using (12), likewise from 5° to 90° in 5° increments.

Making the small-angle approximation for both φ_d and φ_a in (11) yields a closed expression for φ_d :

$$\varphi_d^2 = \varphi_a^2 \left[\frac{1}{2} + \sqrt{\frac{1}{4} + \frac{\text{Bu}\Delta_v}{\text{Ro}\varphi_a^4}} \right] = \varphi_a^2 \left[\frac{1}{2} + \sqrt{\frac{1}{4} + \left(\frac{\varphi_{\text{Ro,ann}}}{\varphi_a} \right)^4} \right]. \quad (12)$$

This is shown as overlaid contours in [Fig. 2](#). Only for $(\text{Bu}\Delta_v/\text{Ro})^{1/4} \geq 0.8$ does the small-angle approximation error exceed a few degrees latitude, irrespective of φ_a .

b. Incorporating theory for φ_a

Using (12) requires knowledge of φ_a , which [KL12](#) diagnose. [Hill et al. \(2021\)](#) derive a prognostic theory for φ_a as determined by the meridional extent of supercritical forcing, based on the following arguments. If no large-scale meridional overturning circulation existed, local radiative-convective equilibrium (RCE) must prevail at each latitude in the time mean. But given the resulting meridional temperature gradients driven by the meridional distribution of insolation, this hypothetical RCE state would generate zonal wind fields through gradient balance that are symmetrically unstable from the equator to some latitude in the summer hemisphere; the presence of this instability defines the tropical supercritical forcing extent ([Plumb and Hou 1992](#); [Emanuel 1995](#)). A large-scale meridional overturning circulation therefore must emerge spanning at least the supercritical latitudes, and in axisymmetric atmospheres that circulation must be the Hadley cells. In eddying atmospheres, in principle the circulation that emerges over the supercritical region could be predominantly macroturbulent as in the extratropics rather

than Hadley-like, but in practice the opposite occurs: the ascending edge latitude is poleward of—and, crucially, proportional to—the supercritical extent.

Formally, in the small-angle limit Hill et al. (2021) show that

$$\varphi_a = c_a \left(\frac{\text{Ro}_{\text{th}}}{2} \right)^{1/3}, \quad (13)$$

where $(\text{Ro}_{\text{th}}/2)^{1/3}$ is the theoretical solution for the supercritical extent and c_a is the empirically determined proportionality constant. Ro_{th} is the thermal Rossby number,

$$\text{Ro}_{\text{th}} \equiv \text{Bu} \Delta_h \sin \varphi_m, \quad (14)$$

with Δ_h the parameter of the imposed forcing (i.e., the latitude-by-latitude RCE state) that—in conjunction with φ_m , the latitude at which the forcing maximizes—determines the bulk meridional temperature gradients of the forcing. The same $\text{Ro}_{\text{th}}^{1/3}$ scaling emerges in the semiempirical, axisymmetric theory of Caballero et al. (2008), as well as (for sufficiently small Ro_{th}) in numerical solutions of the original LH88 axisymmetric, equal-area model of the solstitial Hadley cells (Guendelman and Kaspi 2018). The Hill et al. (2021) scaling (13) emerges from a less strict set of assumptions than Caballero et al. (2008) and presupposes neither axisymmetry nor anything about the resulting circulation's zonal wind and energy transport fields, unlike the equal-area model. Moreover, the solstitial equal-area model (LH88) predicts implausibly large Hadley cells for Earth as φ_m moves more than a few degrees off equator (Hill et al. 2019) and is biased poleward against numerical simulations in an idealized GCM over a wide range of planetary parameter values (cf. Fig. 15a of Guendelman and Kaspi 2019).

For the solstitial, cross-equatorial Hadley cells in the simulations analyzed by Hill et al. (2021) the best-fit value of c_a ranges from 1.3 to 2.6 across three idealized GCMs.⁷ For Ro_{th} , Hill et al. (2021) show that for solstitial seasons one can attain an accurate estimate with φ_m set to 90° by tuning the value of Δ_h . Doing so, the nonstandard $\sin \varphi_m$ term drops out and the Ro_{th} definition becomes the more conventional $\text{Ro}_{\text{th}} = \text{Bu} \Delta_h$. But the $\sin \varphi_m$ dependence is necessary for understanding the annual cycle as will be discussed further below (see also Fig. 15 of Guendelman and Kaspi 2020).

Given diagnosed values of c_a and Ro for each Hadley cell, (13) in conjunction with (12) provide a theory for all three cell edges: (13) predicts φ_a , and using that in (12) for φ_d then yields

$$\varphi_d = c_d c_a \left(\frac{\text{Ro}_{\text{th}}}{2} \right)^{1/3} \sqrt{\frac{1}{2} + \sqrt{\frac{1}{4} + \frac{2^{4/3}}{c_a^4} \frac{\Delta_v}{\Delta_h \sin \varphi_m} \frac{1}{\text{Ro} \text{Ro}_{\text{th}}^{1/3}}}}, \quad (15)$$

⁷ Hill et al. (2021) report values for c_a of 1.0, 1.7, and 2.1 for the Faulk et al. (2017), Singh (2019), and Hill et al. (2021) simulations, respectively, but these implicitly incorporate the $2^{-1/3} \approx 0.8$ factor in (13). We separate it out from c_a for better consistency with (13).

where we have also included the empirical fitting parameter c_d that will prove necessary for the simulations analyzed below. The term $\Delta_v/\Delta_h \sin \varphi_m$, which is the ratio of the planetary-scale vertical to horizontal fractional potential temperature changes of the latitude-by-latitude RCE state, amounts to a seasonally varying bulk isentropic slope of the forcing. From (15), the poleward edge of either Hadley cell increases with increasing Ro_{th} , increasing RCE isentropic slope, or decreasing Ro . Large Ro_{th} corresponds to the large- φ_a limit above, $\varphi_d \approx \varphi_a$, while small Ro_{th} corresponds to the small- φ_a limit of $\varphi_d \approx \varphi_{\text{Ro},\text{ann}}$.

c. Influence of surface thermal inertia on the φ_a seasonal cycle

Because insolation varies seasonally, any nonzero thermal inertia of the surface mixed layer damps and delays the surface thermal response, the more so the larger the mixed layer heat capacity. This is true of the dynamically equilibrated climate but also the hypothetical latitude-by-latitude RCE state that determines φ_a . We therefore now define an “effective” thermal forcing based on the analytical model of Mitchell et al. (2014) which leaves the functional form of (13) for φ_a intact but modifies the φ_m term within Ro_{th} to be damped and delayed in its seasonal excursions. The appendix below provides the derivation, presenting here only the end results of how φ_m is modified.

First consider the unmodified φ_m annual cycle. For Earth's present-day insolation, during equinoctial seasons there is only one maximum in φ_m , but during solstitial seasons there are two maxima in the summer hemisphere, a local one near 44° and the global maximum at the summer pole (see, e.g., Fig. 1 of Hill et al. 2021). Though the polar maximum is relevant for the global-scale Hadley cells in other planetary atmospheres (Singh 2019), for Earth we can comfortably consider the midlatitude maximum at solstice to be φ_m . An advantage of this choice is that, combining the equinoctial and solstitial seasons, this yields a nearly sinusoidal annual cycle of φ_m (not shown): $\varphi_m \approx \varphi_{m,\text{ann}} \cos[\omega_{\text{orb}}(t - t_{\text{solst}})]$, where $\varphi_{m,\text{ann}} = 44^\circ$ is the annual maximum value of φ_m , ω_{orb} is the orbital frequency, t is the time of year, and t_{solst} is the time of year of northern summer solstice.

Next, cf. Mitchell et al. (2014) we define the ratio of the seasonal time scale to the thermal inertial time scale as $\alpha \equiv (\omega_{\text{orb}} \tau_{\text{ti}})^{-1}$, where $\tau_{\text{ti}} = C_{\text{ml}}/(4\sigma \bar{T}^3)$ is the thermal inertia time scale with C_{ml} the surface mixed layer heat capacity, σ the Stefan–Boltzmann constant, and \bar{T} the annual-mean, global-mean temperature. The heat capacity of the mixed layer is given by $C_{\text{ml}} = \rho_w c_w H_{\text{ml}}$, where ρ_w is the density of liquid water, c_w is the heat capacity of liquid water, and H_{ml} is the depth of the mixed layer. Using values of $\rho_w = 1000 \text{ kg m}^{-3}$, $c_w = 4186 \text{ J kg}^{-1} \text{ K}^{-1}$, and taking $H_{\text{ml}} = 10 \text{ m}$ as used in the simulation to be discussed, we have $C_{\text{ml}} \approx 4.186 \times 10^7 \text{ J m}^{-2} \text{ K}^{-1}$. Then using $\bar{T} = 288 \text{ K}$ and $\sigma = 5.67 \times 10^{-8} \text{ W m}^{-2} \text{ K}^{-4}$, the thermal inertia time scale is $\tau_{\text{ti}} \approx 89$ days. Using $\omega_{\text{orb}} = 2\pi/365 \text{ days}^{-1}$ we have $\alpha \approx 0.65$, an intermediate value: the thermal inertial and seasonal cycle time scales are comparable, meaning that the effective φ_m annual cycle will be moderately

damped and phase lagged from the insolation. Cf. the [appendix](#) below, this yields a damping factor to φ_m of $\alpha/\sqrt{1+\alpha^2} \approx 0.55$ and a lag of $\tau_{\text{lag}} = \omega_{\text{orb}}^{-1} \arctan(\alpha^{-1}) \approx 57$ days: roughly, the effective φ_m is damped by half and delayed by two months. These values will prove fairly accurate in predicting φ_a in the simulation discussed next, albeit with the lag empirically reduced by $\sim 20\%$, to 45 days, for a best fit.

For the time scale of φ_d relative to the seasonal cycle, we proceed much more empirically. Insofar as φ_d is determined by the combination of φ_a and Ro as we have posited, one relevant time scale is that of the upper-level zonal wind adjustment: it takes a finite amount of time for the zonal winds in the descending branch to adjust to a change in φ_a in the opposite hemisphere. The other is the time scale of changes in Ro; however, we lack clear intuition for what controls Ro and thus this time scale (see the discussion below for some speculation); moreover a time-invariant Ro seems to fit the simulation well as shown below. We find empirically that the best fit to the simulated φ_d occurs by lagging our predicted φ_d based on the contemporaneous Ro and φ_a by roughly one month, which seems not radically too long nor short.

4. Simulation results

We now assess these theoretical arguments against simulations in three idealized GCMs. After describing the models and simulations, we consider the annual cycles of φ_d and φ_a in an Earthlike aquaplanet control simulation, followed by their behaviors across a wide range of rotation rates in all three GCMs.

a. Description of models and simulations

Details of the model formulations and simulations are provided by [Hill et al. \(2021\)](#). Briefly, the dry model ([Schneider 2004](#)) approximates radiative transfer via Newtonian cooling, with the equilibrium temperature field that temperatures are relaxed toward being the forcing field from [LH88](#) but maximizing at the North Pole (i.e., setting $\varphi_m = 90^\circ$). The relaxation field is statically unstable, and a simple convective adjustment scheme relaxes over a fixed time scale the temperatures of unstable columns toward a lapse rate of $\gamma\Gamma_d$, where $\Gamma_d = g/c_p$ is the dry adiabatic lapse rate with c_p the specific heat of dry air at constant pressure, and $\gamma = 0.7$ mimics the stabilizing effects of latent heat release that would occur in a moist atmosphere (though the model is otherwise dry). Four simulations are performed, three with the Δ_h parameter that determines the horizontal temperature gradients of the forcing set to 1/15 and with the planetary rotation rate set to 0.25, 1, or $2 \times$ Earth's value, and another with $\Delta_h = 1/6$ and Earth's rotation rate. The $\Delta_h = 1/6$ value is conventional ([LH88](#)), but [Hill et al. \(2021\)](#) show that, for $\varphi_m = 90^\circ$, $\Delta_h = 1/15$ is the best fit to numerically simulated latitude-by-latitude RCE.

The moist simulations are those originally presented by [Faulk et al. \(2017\)](#) and [Singh \(2019\)](#). The [Faulk et al. \(2017\)](#) simulations use the idealized aquaplanet model of [Frierson et al. \(2006\)](#) featuring a slab-ocean lower boundary with a 10-m mixed layer depth. They are forced either with an annual cycle of insolation approximating that of present-day Earth or with

insolation fixed at northern summer solstice. The annual cycle simulations include planetary rotation rates ranging from 1/32 to $4 \times$ Earth's by factors of 2, while the three perpetual solstice simulations are at 1, 1/8, or 1/32 \times Earth's rotation rate. The [Singh \(2019\)](#) simulations use an idealized aquaplanet close to that of [O'Gorman and Schneider \(2008\)](#), itself a modified version of the [Frierson et al. \(2006\)](#) model. All of these simulations use a time-invariant, solstitial insolation forcing as in the second subset of the [Faulk et al. \(2017\)](#) simulations, with rotation rates ranging from 1/8 to $8 \times$ Earth's.

The simulated values of φ_d are diagnosed conventionally as the latitude at which the mass-overturning streamfunction at the level of the cell center reaches 10% of its maximum value, with an additional $\cos\varphi$ weighting factor that accounts for constricting latitude circles moving poleward ([Singh 2019](#)). The 10% threshold is needed rather than a zero crossing for cases with large Hadley cells, in which the Ferrel cells and/or summer Hadley cell can be nonexistent and the streamfunction same-signed (albeit very weak) all the way to either pole. For φ_a , the same 10% threshold is used in the perpetual-solstice simulations and in the annual cycle simulations for months in which the summer Hadley cell has effectively vanished. In months where both Hadley cells are well defined, φ_a is taken as the average of the inner edges of the two cells computed using this 10% criterion (which is approximately the latitude of the streamfunction zero crossing; not shown).

b. Annual cycles of φ_a and φ_d

Before presenting the simulation results, we delineate three regimes regarding the relative importance of Ro versus φ_a in determining φ_d . First is where Ro predominates: by [\(12\)](#) if φ_a is small relative to $\varphi_{\text{Ro,ann}} = (\text{Bu}\Delta_v/\text{Ro})^{1/4}$ throughout the annual cycle, then the annual cycle of φ_d is determined by the annual cycle of Ro (provided that Δ_v and H are constant across seasons). Second is intermediate, with both Ro and φ_a influential as in the compensation regarding the winter φ_d found by [KL12](#) in CMIP3 simulations: φ_a is farthest poleward at solstice, acting to move φ_d poleward, but Ro is largest in the solstitial cross-equatorial cell, acting to move the winter φ_d equatorward. Third is where φ_a predominates, as we now show holds for the seasonally forced simulation at Earth's rotation rate of [Faulk et al. \(2017\)](#): φ_a variations (which are well predicted by supercriticality provided thermal inertia is accounted for) with Ro = 1 assumed throughout the annual cycle account for the annual cycle of the winter φ_d .

[Figure 3](#) shows the climatological annual cycles of φ_a (solid red curve), of φ_d in both hemispheres (solid blue curves), and of the meridional overturning streamfunction at 500 hPa (color shading), as well as theoretical estimates described below for each cell edge. The simulated cells are Earthlike in their total meridional extent (φ_d varies over 21.3° – 27.7°N and 21.7° – 26.5°S) and annual cycle phasing, with φ_a migrating into either summer hemisphere with a ~ 1.5 -month lag behind the insolation. However, the φ_a excursions are excessive, 25.7°S – 23.2°N , resulting in an excessively rapid transition from equinoctial to solstitial regimes, approaching closer to

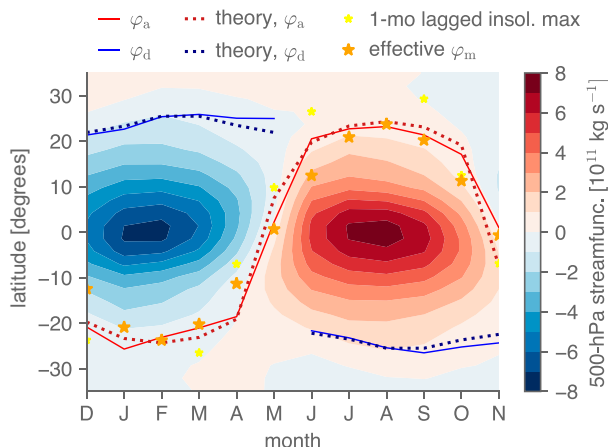


FIG. 3. In the seasonally forced, Earthlike aquaplanet simulation, climatological annual cycle of Hadley cell streamfunction at 500 hPa in shading according to the color bar, as well as Hadley cell edges and theories for the Hadley cell edges as indicated in the legend. The effective φ_m is the effective insolation maximum for that month given the damping and delaying effects of thermal inertia on the seasonally varying forcing. The insolation maximum (yellow stars) is lagged by 1 month from its actual value to facilitate comparison with φ_a , and in the 2 months nearest solstice the maximum is near the summer pole and thus not shown.

the square-wave prediction of LH88 for axisymmetric atmospheres than Earth's more sinusoidal variations (Dima and Wallace 2003).⁸ This results in the summer cell being too weak, such that φ_d is only well defined in the winter half-year for either hemisphere (December–May for the Northern Hemisphere, June–November for the Southern Hemisphere). These discrepancies seem attributable to the rather shallow 10-m surface mixed layer, which promotes excessive seasonality (Donohoe et al. 2014; Wei and Bordoni 2018). Nevertheless, the variations in φ_d and φ_a —in particular that the φ_d ranges are comparable to Earth's and several times smaller than that of φ_a —lead us to consider this useful enough for Earth.

The insolation maximum is near the summer pole during the core solstitial months and within the tropics otherwise (yellow stars, lagged by 1 month to ease comparison with φ_a). The effective φ_m accounting for thermal inertia (orange stars) is damped and lagged from the actual insolation as described above. φ_a stays within the tropics always, with $\varphi_a \approx \varphi_m$ to a reasonable degree. The supercriticality scaling (13) yields an even better prediction (dotted dark red curve), calculated as follows. Hill et al. (2021) perform a 2D parameter sweep of φ_m and Δ_h to determine best fits of the LH88 thermal forcing profile against numerical simulations of latitude-by-latitude RCE under solstitial forcing; for $\varphi_m \approx 44^\circ$ the best fit over the tropics occurs for $\Delta_h = 1/8$ (approximately twice that of the

$\Delta_h = 1/15$ value for $\varphi_m = 90^\circ$).⁹ We therefore take $\Delta_h = 1/8$. With Δ_h set, the proportionality constant c_a is left effectively as a fitting parameter, which by eye provides the best fit for $c_a \approx 1.9$.¹⁰ The prediction is clearly not without empiricism, but nevertheless, we are pleased with the overall accuracy against the simulated φ_a .

We then use this theoretically computed φ_a as just described to predict φ_d . Due to an inadvertent loss of zonal-wind data from the Faulk et al. (2017) simulations, we are not able to directly diagnose Ro. Instead, we assume Ro = 1, which provided $0 \leq \text{Ro} \leq 1$ yields the equatorward-most possible φ_d predictions, all else equal. Even still, this yields a φ_d prediction poleward of the simulated φ_d values (not shown), which we correct for by setting $c_d = 0.75$ in (15). We then shift the results later in time by one month, resulting in a fairly accurate fit to the simulations (dotted blue curve). In the concluding section below we provide speculative arguments to justify this equatorward displacement and 1-month phase lag of φ_d compared to φ_a (which in turn lags the insolation by ~ 1.5 months). The φ_d prediction is only marginally improved if the actual simulated φ_a values are used rather than our predicted φ_a (not shown).

Because the monthly variations of φ_d are comparable to those of the comprehensive GCMs shown by KL12 ($\leq 5^\circ$ about their annual means), we infer that muted annual cycles of φ_d relative to that of φ_a can emerge via different mechanisms even restricting to Earthlike conditions. On the one hand are the comprehensive GCMs analyzed by KL12: the seasonal Ro values (that KL12 indirectly diagnose as a fitting parameter) span 0.45–1, and φ_a presumably varies closer to the real-world value and thus less than in our aquaplanet simulations. On the other hand is our aquaplanet simulation: φ_d variations (provided c_d and the 1-month lag from φ_a are accounted for) appear determined almost entirely by the seasonality of φ_a with Ro treated as constant.

The theoretical predictions are also relatively insensitive to a reasonable range of parameter values. By (12), using conventional values of $H = 10$ km and $\Delta_v = 1/8$, then for Earth $\text{Bu} \approx 0.46$ and $\text{Bu}\Delta_v \approx 0.06$. Then varying φ_a over 0° – 15° , and Ro over the KL12-reported Ro range of 0.45–1 yields a φ_d range of 28.0° to 35.9° (for $\varphi_a = 0$, Ro = 1 and $\varphi_a = 15^\circ$, Ro = 0.45, respectively). Moreover, the φ_d range is fairly insensitive to Ro if φ_a is held fixed and likewise to φ_a if Ro is held fixed: if

⁹ For the annual-mean rather than solstitial RCE state, Hill et al. (2020) diagnose a similar $\Delta_h \approx 1/8$ value based on numerical RCE simulations under annual-mean insolation. This value is considerably larger than the solstitial one, which suggests that Δ_h would be even larger under equinoctial forcing. But we do not attempt to account for this seasonality in Δ_h .

¹⁰ This value of c_a is $\sim 45\%$ larger than the best-fit value of 1.31 (Hill et al. 2021) for the solstitial φ_a across the Faulk et al. (2017) seasonally forced simulations with different rotation rates—a neither trivial nor order-of-magnitude difference, suggesting that the proportionality is moderately influenced by different processes in these two distinct contexts. The 1.9 value is also less than the values of 2.2 and 2.6 diagnosed across rotation rates for, respectively, the simulations of Singh (2019) and the dry simulations of Hill et al. (2021).

⁸ In fact the annual-mean rainfall and Hadley cells both show a double ITCZ resulting from this rapid jumping of the ascent fairly deep into either summer hemisphere (not shown).

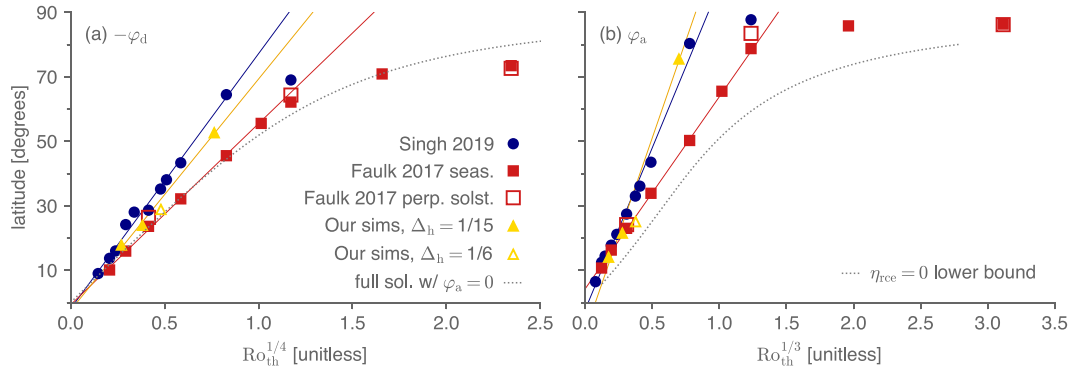


FIG. 4. (a) Latitude of the winter hemisphere descending edge of the cross-equatorial Hadley cell, φ_d , in idealized aquaplanet simulations of [Faulk et al. \(2017\)](#) and [Singh \(2019\)](#), and in the idealized dry simulations of [Hill et al. \(2021\)](#) as a function of the thermal Rossby number to the one-fourth power, each signified by different symbols as indicated in the legend. The solid lines show the linear best fit for φ_d as a function of $\text{Ro}_{\text{th}}^{1/4}$ for the given simulation set, restricting to $\text{Ro}_{\text{th}} < 1$, with red, blue, and yellow for the [Singh \(2019\)](#), [Faulk et al. \(2017\)](#), and the $\Delta_h = 1/15$ dry simulations, respectively. The dotted gray curve is the numerical solution to (11) with $\varphi_a = 0$ and $\text{Ro}\Delta_h/\Delta_v = 1$. (b) The corresponding quantities for the summer, ascending edge φ_a , with the horizontal axis spacing being $\text{Ro}_{\text{th}}^{1/3}$, and the dashed gray curve being the numerical solution to the full expression for the extent of supercritical forcing [(b) replicates Fig. 6 of [Hill et al. \(2021\)](#)].

Ro is fixed at unity, the $\varphi_a = 15^\circ$ prediction moves equatorward only by 1.7° , and conversely if φ_a is at the equator the $\text{Ro} = 0.45$ prediction moves poleward by only 2.1° .

c. Relative behaviors of solstitial φ_a and φ_d across rotation rates

From (13), $\varphi_a \propto \text{Ro}_{\text{th}}^{1/3}$, which [Hill et al. \(2021\)](#) show accurately describes the solstitial φ_a across planetary rotation rates in the simulations presently under consideration. For φ_d , by (11) for small Ro_{th} and thus small φ_a ,

$$\varphi_d \approx c_d \left(\frac{\text{Bu}\Delta_v}{\text{Ro}} \right)^{1/4} = c_d \left(\frac{\text{Ro}_{\text{th}}}{\text{Ro}} \frac{\Delta_v}{\Delta_h} \right)^{1/4}, \quad (16)$$

again incorporating the empirical fitting parameter c_d . In that case, provided Ro does not change appreciably then $\varphi_d \propto \text{Bu}^{1/4} \sim \text{Ro}_{\text{th}}^{1/4}$, where in this context we can substitute Ro_{th} for Bu since only Ω is varied and appears identically (as Ω^{-2}) in the two nondimensional numbers. We now argue that the idealized GCM simulations reflect this modest $1/3 - 1/4 = 1/12$ difference in power-law exponent in Ro_{th} for φ_a versus φ_d .

[Figure 4a](#) shows the winter φ_d for all the simulations as a function of $\text{Ro}_{\text{th}}^{1/4}$. For each model, a best-fit line is included of φ_d with $\text{Ro}_{\text{th}}^{1/4}$, restricting to simulations in the linear regime of φ_d versus $\text{Ro}_{\text{th}}^{1/4}$.¹¹ Overall the simulations follow this scaling well. [Table 1](#) lists the slope and intercept from the linear best fits of φ_d against $\text{Ro}_{\text{th}}^{1/4}$, with the slope amounting to a best fit for the empirical c_d parameter in (15) (at least in the

small- Ro_{th} limit). The inferred c_d values range from 1.4 for the [Singh \(2019\)](#) simulations to 0.9 for the [Faulk et al. \(2017\)](#) perpetual solstice simulations. The value of 1.0 for the [Faulk et al. \(2017\)](#) seasonal cycle simulations is modestly higher than the value discussed above of 0.8 for the climatological annual cycle in the [Faulk et al. \(2017\)](#) simulation at Earth's rotation rate—opposite to c_a , which was larger for the annual cycle than across rotation rates. The intercepts, which in theory should be zero, range from -2.4° to 5.6° latitude and average across the simulation sets to a modest 0.3° .

[Table 1](#) includes best-fit power-law exponents for φ_d and for φ_a against Ro_{th} computed for each set of simulations by linear regression in log-log space. For all sets of simulations, the inferred exponent is larger and closer to $1/3$ for φ_a than for φ_d , which is closer to $1/4$. The dry simulations exhibit the largest exponents for both, 0.41 and 0.3, respectively, and the [Faulk et al. \(2017\)](#) seasonally forced and perpetual-solstice simulations, respectively, give the smallest exponents, 0.28 and 0.21. The average of the best-fit exponents across the four simulation sets are nearly identical to the scalings, 0.26 and 0.33.

As Ro_{th} increases beyond ~ 1 , the simulated φ_d level off, never exceeding $\sim 70^\circ$. The full, non-small-angle expression (11) solved numerically with $\varphi_a = 0$ and all parameters except Ω set to Earthlike values (dotted gray curve) qualitatively captures this. This contrasts with φ_a —shown in [Fig. 4b](#) as a function of $\text{Ro}_{\text{th}}^{1/3}$ (reproducing Fig. 6 of [Hill et al. \(2021\)](#))—which in the slowly rotating regime is near the summer pole ([Hill et al. \(2021\)](#)). In other words, as rotation rate decreases the cross-equatorial Hadley cell becomes increasingly lopsided, in the slowly rotating regime extending effectively to the summer pole but not the winter pole. As noted above, the solutions (11) and (12) for φ_d always predict $|\varphi_d| \geq |\varphi_a|$, and as such to explain the $|\varphi_d| < |\varphi_a|$ cases we must appeal to the empirical proportionality constants c_a and c_d introduced in (13) and (15) as follows.

¹¹ The extents of this linear regime (as well as the individual φ_a and φ_d values) differ appreciably between the two moist models, which are very similarly formulated, for reasons we do not understand. It spans $\text{Ro}_{\text{th}} \lesssim 1$ for the [Singh \(2019\)](#) simulations vs $\text{Ro}_{\text{th}} \lesssim 1.5$ for the [Faulk et al. \(2017\)](#) simulations.

TABLE 1. Best-fit exponents of power-law scalings for the winter and summer edges of the cross-equatorial solstitial Hadley cell in each set of simulations, as well as the best-fit slope and intercepts for each simulation set against the theoretical Ro_{th} power law. The slope for φ_d amounts to an approximation of c_d and that of φ_a an approximation of c_a ; the latter is reported with the additional $2^{-1/3}$ factor included to facilitate direct comparison with c_d . Simulations are restricted to those for which $Ro_{th} < 2$, since the theoretical predictions of 1/3 and 1/4 for the winter and summer edges, respectively, assume small angle and thus small Ro_{th} . The dry LH88-forced simulations do not include the $\Delta_h = 1/6$ case. S19 stands for Singh (2019), and F17 stands for Faulk et al. (2017). The last row lists the diagnosed c_d and c_a values for the annual cycle in the Faulk et al. (2017) Earthlike simulation.

	Winter φ_d			Summer φ_a		
	Power	c_d	Intercept	Power	$c_a/2^{1/3}$	Intercept
Theory	0.25	—	0°	0.33	—	0°
S19	0.28	1.4	-1.9°	0.34	1.8	-2.3°
F17, seasonal forcing	0.26	0.9	0.2°	0.28	1.1	4.0°
F17, perpetual solstice	0.21	0.9	5.7°	0.30	1.1	4.4°
Dry, LH88 forced	0.26	1.3	-2.4°	0.41	2.1	-9.2°
F17, annual cycle	—	0.8	—	—	1.9	—

If Ro and the forcing isentropic slope Δ_v/Δ_h are both approximately unity, it can be shown from (13) and (16) that $\varphi_a = \varphi_d$ provided that $2^{1/3}c_d/c_a = Ro_{th}^{1/2}$. Table 1 includes the slope and intercepts of φ_a against $Ro_{th}^{1/3}$, with the slope amounting to a best fit for $c_d/2^{1/3}$ in (13). From Table 1 then, the ratio $2^{1/3}c_d/c_a$ takes values approximately over 0.6–1 in the four simulation sets. Given the 0.6–1 range for the left-hand side, this yields $Ro_{th} \approx 1$, with φ_d equatorward of φ_a for larger Ro_{th} . This roughly captures the behavior of the simulations. Of course, the slowly rotating regime with $|\varphi_a| > |\varphi_d|$ extends beyond the regime where the small-angle power-law scalings being appealed to are credible, but it nevertheless begins within the small-angle regime.

The unfilled yellow triangle in Fig. 4 shows the dry, LH88-forced simulation at Earth’s rotation rate with $\Delta_h = 1/6$ rather

than $\Delta_h = 1/15$ as in the other three dry simulations. As is the case for φ_a (Hill et al. 2021), φ_d is somewhat separated from the power law of the $\Delta_h = 1/15$ cases. Strictly speaking, in the $\varphi_a \approx 0$ limit of (11), φ_d is independent of Δ_h . But, while small, $\varphi_a \neq 0$ in the simulations, and since an increase in Δ_h moves φ_a poleward, it is qualitatively consistent that φ_d moves poleward as a result. Given that the annual cycle amounts to a variation in $\Delta_h \sin \varphi_m$, it is worth noting that the slope between the $\Delta_h = 1/15$ and $\Delta_h = 1/6$ cases at Earth’s rotation rate is shallower than that inferred across rotation rates at $\Delta_h = 1/15$, which qualitatively coheres with c_d being smaller for the annual cycle than across rotation rates in the Faulk et al. (2017) simulations (Table 1). A caveat, however, is that the deviation of the $\Delta_h = 1/6$ case is modest; whether $\Delta_h = 1/6$ cases at

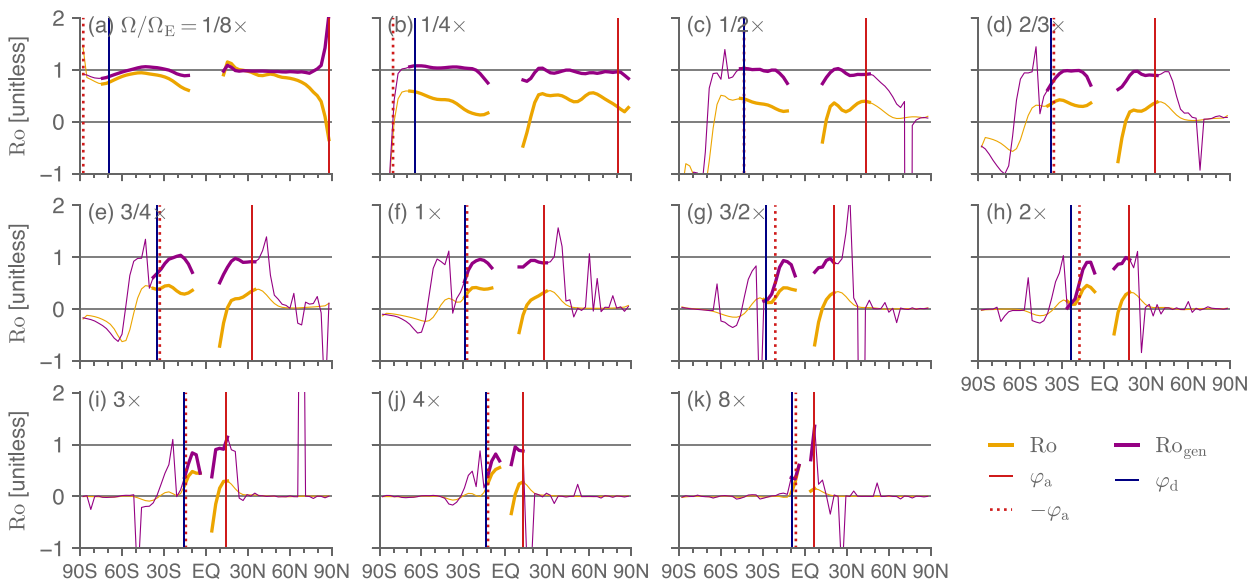


FIG. 5. Rossby number in the Singh (2019) simulations at the 300-hPa level, computed either conventionally using (3) or the generalized form (17) that accounts for the tilting of streamlines. Overlaid are the cell edges φ_a and φ_d , with $-\varphi_a$ also shown to ease comparison of the relative poleward extents of the Hadley circulation are shown as thinner curves, since they are less relevant. They are also masked near the equator where division by the Coriolis parameter makes them less meaningful, within 12° on either side for the slowest rotation rate and by 1° less on either side for each subsequent rotation rate.

different rotation rates or other Δ_n values would actually yield a different slope remains an open question.

d. Validity of the uniform-Ro assumption

Finally, we assess the validity of treating the upper-tropospheric Ro as uniform within each Hadley cell. Figure 5 shows the meridional profile of Ro at 300 hPa in each simulation of Singh (2019), computed both conventionally as (3) and, following Singh (2019), in a generalized form that incorporates vertical advection of angular momentum:

$$\text{Ro}_{\text{gen}} \equiv \frac{1}{f} \left[-\zeta + \frac{\omega}{v} \frac{\partial u}{\partial p} \right], \quad (17)$$

where v is meridional velocity, ω is vertical velocity in pressure coordinates, p is pressure, and all quantities are zonal averages. This accounts for the considerable tilting of streamlines in the upper branch of the cross-equatorial cells [cf. Figs. 3 and 4 of Faulk et al. (2017), Fig. 7 of Singh (2019), and Fig. 5 of Hill et al. (2021)], which causes the conventional Ro to deviate from unity even if streamlines and angular momentum contours are everywhere parallel. Though it is the conventional Ro that appears in u_{Ro} and thus ultimately our expressions for φ_d , for the simulations we argue that (17) is more instructive: for the two-layer model of baroclinic instability utilized, the bulk upper-tropospheric behavior is more relevant than that at any chosen pressure level. And as streamlines begin tilting toward the surface in the descending branch, the conventional Ro at any given level decreases, while the bulk zonal velocities of the upper branch still roughly correspond to the planetary angular momentum values from where the streamlines exited the boundary layer in the ascending branch. In other words, along streamlines angular momentum is nearly conserved (see Fig. 7 of Singh 2019), which the meridional profile of Ro at a fixed pressure level cannot capture.

The generalized Rossby number is close to unity over a large fraction of the cross-equatorial Hadley cell extent in all cases. (Both forms are masked out near the equator, as specified in the caption, where division by the Coriolis parameter makes them less physically meaningful.) The difference made by the vertical advection term is particularly large in the ascending branches. For either version, we subjectively identify two regimes over the descending branch. Slowly rotating cases have Ro_{gen} relatively uniform or even increasing slightly from the equator to the winter descending edge. More rapidly rotating cases have Ro_{gen} decreasing poleward, approaching zero in the vicinity of the winter descending edge, but there is considerable scatter in the value of Ro_{gen} at the edge. Despite this variation in the Rossby number across the simulations, it is evidently small enough that taking the bulk Ro_{gen} value as fixed in our scalings does not introduce major error.

5. Conclusions

a. Summary

We have introduced a unified theory for the latitudes of all three Hadley cell edges—the equatorward, ascending edge (φ_a) shared by the two Hadley cells as well as each cell's poleward, descending edge (φ_d)—throughout the annual cycle by

combining two previous theories. First we predict φ_a using our recent theory based on the meridional extent of low-latitude supercritical forcing (Hill et al. 2021). We then essentially plug this φ_a into the theory for φ_d based on baroclinic instability onset of KL12 that uses the seasonally varying φ_a and an assumed uniform Rossby number (Ro) within each Hadley cell's upper branch. The new theory predicts that φ_d is displaced poleward when Ro decreases or as φ_a moves poleward, and φ_a varies with the thermal Rossby number (Ro_{th}) to the one-third power. But in the small-angle limit reasonable for Earth, the dependence on φ_a drops out and the scaling for φ_d predicts a one-fourth power dependence on the planetary Burger number, or equivalently on Ro_{th} if only the planetary rotation rate (or any other term appearing in both Bu and Ro_{th}) are varied. The mixed layer's thermal inertia acts to damp and delay φ_a relative to the insolation annual cycle, which we account for via an “effective” forcing annual cycle based on the formalism of Mitchell et al. (2014).

In an Earthlike, seasonally forced idealized aquaplanet simulation with a relatively shallow, 10-m mixed layer ocean depth, φ_a migrates rapidly to $\sim 25^\circ$ into either summer hemisphere, and this seasonal cycle is well captured by the supercriticality-based scaling. The summer cell is too weak for the summer φ_d to be meaningful, but the winter φ_d varies by only $\leq 5^\circ$ latitude about its mean position in either hemisphere. Our combined theory predicting φ_a and φ_d captures this behavior with Ro kept at unity as in the original H00 model, but requires in place of Ro variations that the φ_d prediction be lagged by 1 month from that of φ_a —which in turn is lagged by ~ 1.5 months from the insolation.

In simulations across a wide range of planetary rotation rates in three idealized GCMs, both φ_d and φ_a adhere to the respective power-law exponents predicted by our theory in the relevant small thermal Rossby number regime. This, combined with a smaller proportionality constant for φ_d compared to φ_a , helps explain why at very slow rotation rates the solstitial Hadley cell ascends essentially at the summer pole but descends considerably equatorward of the winter pole, $\sim 70^\circ$, rather than being roughly symmetric in extent about the equator as for more rapidly rotating cases including Earth.

b. Discussion

How might a predictive theory for Ro be constructed? Hoskins et al. (2020) offer an intriguing perspective relating to the frequency of deep convection in the ascending branch. They argue that only when convection is sufficiently deep will there be upper-tropospheric meridional outflow that travels nearly inviscidly (i.e., with $\text{Ro} \approx 1$) toward either pole; at times and longitudes where deep convection is absent, they argue $\text{Ro} \approx 0$. Under those conditions, the time-mean, zonal-mean Ro field becomes a function of the spatial and temporal occurrence of deep convection in the ascending branch. This contrasts with the conventional, extratropically focused approach to Ro, wherein it is controlled by stresses from subtropical and extratropical eddies propagating into the deep tropics and breaking (Walker and Schneider 2006; Schneider 2006).

Vallis et al. (2015) speculate that Rossby waves are generated at the latitude of baroclinic instability onset, that these Rossby waves then propagate equatorward and break, and that the Hadley cell terminates at this wave-breaking latitude rather than the instability onset latitude. This equatorward displacement may relate to our need for the $c_d < 1$ parameter value to fit the φ_d annual cycle in the seasonally forced aquaplanet simulation. And this additional step—with some finite time scale required for the overall process of Rossby wave development, propagation, and breaking—could contribute to the lag of φ_d relative to φ_a in the Earthlike seasonal cycle simulation. At the same time, across rotation rates the best fit c_d parameters exceed unity in some cases (Table 1), which is harder to square with this Rossby wave-based mechanism of Vallis et al. (2015).

The physical credibility of the two-layer model's critical shear criterion for baroclinic instability has been fairly questioned; a series of studies utilize a more comprehensive treatment of baroclinic instability to argue that φ_d occurs where the vertical extent of baroclinic eddies spans a sufficient fraction of the troposphere (Korty and Schneider 2008; Levine and Schneider 2011, 2015). The same studies also incorporate the influence of moisture on the effective static stability Δ_v (Levine and Schneider 2011, 2015).

Though we have relied on Ro being uniform over the upper branch of each Hadley cell (cf. KL12), the baroclinic instability criterion is computed latitude by latitude, and as such strictly speaking the behavior of Ro equatorward of the instability onset latitude is irrelevant. This contrasts with the equal-area model appropriate for axisymmetric atmospheres, which depends on the meridional integral of the difference between the RCE and dynamically equilibrated potential temperature fields over the expanse of the cell. In principle one could solve the equal-area model with our fixed-Ro temperature field (6) as a means of indirectly introducing eddy influences into it.

Under annual-mean forcing in two dry and one moist idealized GCM, Mitchell and Hill (2021) find that φ_d scales as $\Omega^{-1/3}$ in all three models. This could be squared with our $\Omega^{-1/4}$ scaling for $\varphi_a = 0$ if Ro scales as $\Omega^{-2/3}$. By eye from their Figs. 8 and 10, Ro does indeed follow an exponent close to this in two of the models—the same dry GCM we use and the moist GCM used by Faulk et al. (2017). But a simpler dry dynamical core (Held and Suarez 1994) shows no clear dependence of Ro on Ω . Mitchell and Hill (2021) also put forward an “omega governor” mechanism which operates in the case that static stability and the effective heating (diabatic plus eddy heat flux convergence) averaged over the descending branch do not change. Under those conditions, the poleward extent and mass overturning rate of the Hadley cell must vary in tandem: the cell weakens if it narrows, and it widens if it strengthens. Prior to any adjustment by φ_d , if φ_a moves poleward then the cell widens, which under the omega governor would act to strengthen the overturning. One can imagine that strengthening causing Ro to increase, insofar as parcels then traverse the upper branch more rapidly and hence are less exposed to eddy stresses. The increase in Ro would, all else equal, act to move φ_d equatorward, countering the direct

influence of φ_a moving poleward. (This apparently is not important for the annual cycle simulation discussed above where Ro = 1 throughout the annual cycle perform suitably.)

The Mitchell et al. (2014) model we use for the effective forcing annual cycle in the presence of thermal inertia is based on radiative equilibrium rather than RCE. It also considers only the equilibration of the ocean surface mixed layer rather than the coupled near-surface atmosphere–ocean. Cronin and Emanuel (2013) derive expressions for the time scale of equilibration to the RCE state in a coupled ocean–atmosphere column but do not consider the latitudinally nor seasonally varying problem. It could be useful to combine these approaches, ideally arriving at an analytical model for the effective seasonally varying forcing for moist atmospheres.

Our theory could be further tested in numerous ways: against reanalysis data for the climatological annual cycle of the Hadley cells, against reanalysis data for interannual variability and trends, against comprehensive climate model simulations of global warming (cf. KL12), and against simulations of other terrestrial planetary atmospheres. For the global warming problem, a useful starting point would be diagnosing seasonal, climatological best-fit Ro and φ_a values for each Hadley cell across comprehensive GCMs in preindustrial simulations in the CMIP6 archive. These could then be compared to diagnosed φ_d climatological values in the same simulations and forced changes in CMIP6 simulations under increased CO₂, although care must be taken in interpreting, e.g., changes in Δ_h , which is strictly a parameter of the hypothetical latitude-by-latitude RCE state, not the dynamically equilibrated state that the archived simulations represent. We look forward to such tests.

Acknowledgments. We are grateful to Sean Faulk and Martin Singh for sharing the data from their simulations and for many valuable discussions. We thank Ilai Guendelman and three anonymous reviewers for helpful comments. S.A.H. acknowledges financial support from NSF Award 1624740 and from the Monsoon Mission, Earth System Science Organization, Ministry of Earth Sciences, Government of India. J.L.M. acknowledges funding from the Climate and Large-Scale Dynamics program of the NSF, Award 1912673.

Data availability statement. Data from the Singh (2019) simulations are available for download at Singh (2021). Data from the Faulk et al. (2017) simulations are available for download at Faulk (2021). Data from the Hill et al. (2021) simulations are available for download at Hill (2021).

APPENDIX

Model of Effective Insolation Annual Cycle Given Surface Thermal Inertia

Here we present the analytical model of Mitchell et al. (2014) for, given nonzero surface thermal inertia, the “effective” annual cycle of radiative-equilibrium temperatures, which are damped and lagged from the insolation (see also appendix A of Lee and Mitchell 2021). The notation and derivations are slightly modified—most notably,

we use real numbers throughout rather than using complex numbers to represent annual oscillations—but the model is ultimately identical to that of Mitchell et al. (2014).

We take insolation S to vary with $\sin^2 \varphi$ from a maximum latitude φ_m that varies over the annual cycle:

$$\frac{S(\varphi, t)}{S_0} = 1 + \frac{\Delta_s}{3} - \Delta_s [\sin^2 \varphi - 2 \sin \varphi_m(t) \sin \varphi], \quad (\text{A1})$$

where Δ_s controls the fractional horizontal gradients in insolation. At any given time, this expression amounts to the forcing from LH88 but with the $\sin^2 \varphi_m$ term omitted [it is also the same functional form as the seasonally varying Newtonian cooling temperature profile of Schneider and Bordonì (2008)]. Omitting that term does not alter the gradient-balanced wind and hence the φ_a prediction, but it makes the resulting derivations easier.

We then take φ_m to vary sinusoidally in time: $\sin \varphi_m = \mu_{m, \text{ann}} \sin(\omega_{\text{orb}} t)$, where ω_{orb} is the orbital frequency, t is the time of year relative to boreal fall equinox, $\mu_{m, \text{ann}} = \sin \varphi_{m, \text{ann}}$, with $\varphi_{m, \text{ann}} = 44^\circ$ being the annual maximum value of φ_m . Thus,

$$\frac{S(\varphi, t)}{S_0} = 1 + \frac{\Delta_s}{3} - \Delta_s [\sin^2 \varphi + 2 \mu_{m, \text{ann}} \sin(\omega_{\text{orb}} t) \sin \varphi]. \quad (\text{A2})$$

As noted by Mitchell et al. (2014), this results in the annual mean at each latitude being independent of the seasonality (i.e., of φ_m and ω_{orb}): denoting annual averages by overbars, we have $\bar{S}/S_0 = 1 + \Delta_s/3 - \Delta_s \sin^2 \varphi$.

We assume an ocean surface mixed layer of uniform depth with heat capacity C_{ml} , whose temperature evolution at each latitude is determined purely by radiative fluxes, warmed by the seasonally varying insolation, and cooled by longwave emission:

$$C_{\text{ml}} \frac{dT}{dt} = S - \sigma T^4, \quad (\text{A3})$$

where σ is the Stefan–Boltzmann constant and T is the mixed layer temperature. This implicitly treats the albedo as uniformly zero; a uniform, nonzero albedo could be incorporated by simply rescaling S_0 . In the annual average at each latitude we then have $\bar{S} = \sigma \bar{T}^4$. Defining $T_0 \equiv (S_0/\sigma)^{1/4}$ and taking $\Delta_s \ll 1$, this yields the familiar $\bar{T}/T_0 = 1 + \Delta_h/3 - \Delta_h \sin^2 \varphi$ (e.g., Held and Hou 1980), having defined $\Delta_h \equiv \Delta_s/4$. [Note that S_0 and T_0 are global parameters but not the global-mean values; global-mean insolation is $S_0(1 + \Delta_s/3)$ and global-mean temperature $T_0(1 + \Delta_h/3)$.]

We now split the insolation and surface temperature into annual-mean and annually varying components at each latitude: $S = \bar{S} + S'$ and $T = \bar{T} + T'$. We assume that $|T'/\bar{T}| \ll 1$, such that $T^4 = (\bar{T} + T')^4 \approx \bar{T}^4 + 4\bar{T}^3 T'$ via Taylor expansion. Then, defining the thermal inertia time scale, (A3) becomes

$$\frac{dT'}{dt} + \frac{T'}{\tau_{\text{ti}}} = \frac{S'}{C_{\text{ml}}}. \quad (\text{A4})$$

We then nondimensionalize (A4), with nondimensional quantities in hats, as $T' = T_0 \hat{T}$, $S' = S_0 \hat{S}$, and $t = \omega_{\text{orb}}^{-1} \hat{t}$. In that case, (A4) becomes

$$\omega_{\text{orb}} T_0 \frac{d\hat{T}}{d\hat{t}} + \frac{T_0}{\tau_{\text{ti}}} \hat{T} = \frac{S_0}{C_{\text{ml}}} \hat{S}. \quad (\text{A5})$$

Next, we define the ratio of the seasonal time scale to the thermal inertia time scale as $\alpha \equiv (\omega_{\text{orb}} \tau_{\text{ti}})^{-1}$. Dividing through by $\omega_{\text{orb}} T_0$, using $S_0/T_0 = \sigma T_0^3$, recalling $\tau_{\text{ti}} = C_{\text{ml}}/4\sigma \bar{T}^3$, and approximating $\bar{T} \approx T_0$, we have

$$\frac{d\hat{T}}{d\hat{t}} + \alpha \hat{T} = \frac{\alpha}{4} \hat{S}. \quad (\text{A6})$$

Denoting $\beta \equiv 2\Delta_s \mu_{m, \text{ann}} \sin \varphi$, then $\hat{S} = -\beta \sin \hat{t}$ and thus

$$\frac{d\hat{T}}{d\hat{t}} + \alpha \hat{T} = -\frac{\alpha \beta}{4} \sin \hat{t}. \quad (\text{A7})$$

This ordinary differential equation has the solution of

$$\hat{T}(\hat{t}) = -\frac{1}{4} \frac{\alpha \beta}{1 + \alpha^2} [\alpha \sin \hat{t} - \cos \hat{t}] + c \exp(-\alpha \hat{t}), \quad (\text{A8})$$

and we set the constant $c = 0$ since the solution is bounded for $\hat{t} \rightarrow -\infty$. This difference between a sine and cosine of the same wavelength amounts to a damped and phase-lagged sine as follows. Denoting the nondimensional phase lag $\hat{\tau}_{\text{lag}}$, by trigonometric identity $\sin(\hat{t} - \hat{\tau}_{\text{lag}}) = \cos \hat{\tau}_{\text{lag}} \sin \hat{t} - \sin \hat{\tau}_{\text{lag}} \cos \hat{t}$. Setting this equal to $\gamma(\alpha \sin \hat{t} - \cos \hat{t})$, where γ is a constant to be determined, implies $\sin \hat{\tau}_{\text{lag}} = \gamma$ and $\cos \hat{\tau}_{\text{lag}} = \alpha \gamma$, and therefore that $\hat{\tau}_{\text{lag}} = \arctan(\alpha^{-1})$. Then, requiring $\sin^2 \hat{\tau}_{\text{lag}} + \cos^2 \hat{\tau}_{\text{lag}} = 1$ yields $\gamma = (1 + \alpha)^{-1/2}$. Thus,

$$\hat{T}(\hat{t}) = -\frac{1}{4} \frac{\alpha \beta}{\sqrt{1 + \alpha^2}} \sin(\hat{t} - \hat{\tau}_{\text{lag}}), \quad \hat{\tau}_{\text{lag}} = \arctan(\alpha^{-1}). \quad (\text{A9})$$

For large α , thermal inertia is weak relative to the annual cycle, yielding $\hat{\tau}_{\text{lag}} \approx 0$ and $\alpha/\sqrt{1 + \alpha^2} \approx 1$: the temperatures are nearly undamped and in phase and with the insolation. For $\alpha \ll 1$, thermal inertia is relatively strong, yielding $\hat{\tau}_{\text{lag}} \approx \pi/2$ and $\alpha/\sqrt{1 + \alpha^2} \approx \alpha$: the temperatures are strongly damped (by a factor of α) and in quadrature with the insolation.

Finally, for completeness the dimensional form of the full seasonally varying, radiative-equilibrium temperature field is

$$\frac{T(t)}{T_0} = 1 + \frac{\Delta_h}{3} \left\{ 1 - 3 \sin^2 \varphi + 6 \frac{\alpha}{\sqrt{1 + \alpha^2}} \mu_{m, \text{ann}} \sin \varphi \sin[\omega_{\text{orb}}(t - \tau_{\text{lag}})] \right\}, \quad (\text{A10})$$

$$\tau_{\text{lag}} = \omega_{\text{orb}}^{-1} \arctan(\alpha^{-1}).$$

REFERENCES

- Adam, O., T. Bischoff, and T. Schneider, 2016: Seasonal and interannual variations of the energy flux equator and ITCZ. Part I: Zonally averaged ITCZ position. *J. Climate*, **29**, 3219–3230, <https://doi.org/10.1175/JCLI-D-15-0512.1>.
- Becker, E., G. Schmitz, and R. Geprags, 1997: The feedback of midlatitude waves onto the Hadley cell in a simple general circulation model. *Tellus*, **49A**, 182–199, <https://doi.org/10.3402/tellusa.v49i2.14464>.

- Bordoni, S., and T. Schneider, 2008: Monsoons as eddy-mediated regime transitions of the tropical overturning circulation. *Nat. Geosci.*, **1**, 515–519, <https://doi.org/10.1038/ngeo248>.
- Byrne, M. P., and R. Thomas, 2019: Dynamics of ITCZ width: Ekman processes, non-Ekman processes, and links to sea surface temperature. *J. Atmos. Sci.*, **76**, 2869–2884, <https://doi.org/10.1175/JAS-D-19-0013.1>.
- Caballero, R., R. T. Pierrehumbert, and J. L. Mitchell, 2008: Axisymmetric, nearly inviscid circulations in non-condensing radiative-convective atmospheres. *Quart. J. Roy. Meteor. Soc.*, **134**, 1269–1285, <https://doi.org/10.1002/qj.271>.
- Cronin, T. W., and K. A. Emanuel, 2013: The climate time scale in the approach to radiative-convective equilibrium. *J. Adv. Model. Earth Syst.*, **5**, 843–849, <https://doi.org/10.1002/jame.20049>.
- Davis, N. A., and T. Birner, 2022: Eddy-mediated Hadley cell expansion due to axisymmetric angular momentum adjustment to greenhouse gas forcings. *J. Atmos. Sci.*, **79**, 141–159, <https://doi.org/10.1175/JAS-D-20-0149.1>.
- Dima, I. M., and J. M. Wallace, 2003: On the seasonality of the Hadley cell. *J. Atmos. Sci.*, **60**, 1522–1527, [https://doi.org/10.1175/1520-0469\(2003\)060<1522:OTSOTH>2.0.CO;2](https://doi.org/10.1175/1520-0469(2003)060<1522:OTSOTH>2.0.CO;2).
- Donohoe, A., D. M. W. Frierson, and D. S. Battisti, 2014: The effect of ocean mixed layer depth on climate in slab ocean aquaplanet experiments. *Climate Dyn.*, **43**, 1041–1055, <https://doi.org/10.1007/s00382-013-1843-4>.
- Emanuel, K. A., 1995: On thermally direct circulations in moist atmospheres. *J. Atmos. Sci.*, **52**, 1529–1534, [https://doi.org/10.1175/1520-0469\(1995\)052<1529:OTDCIM>2.0.CO;2](https://doi.org/10.1175/1520-0469(1995)052<1529:OTDCIM>2.0.CO;2).
- Faulk, S., 2021: Output from the Faulk, Bordoni, and Mitchell 2017 J. Atmos. Sci. idealized aquaplanet simulations, version 1. Zenodo, accessed 21 December 2021, <https://doi.org/10.5281/ZENODO.5796259>.
- , J. Mitchell, and S. Bordoni, 2017: Effects of rotation rate and seasonal forcing on the ITCZ extent in planetary atmospheres. *J. Atmos. Sci.*, **74**, 665–678, <https://doi.org/10.1175/JAS-D-16-0014.1>.
- Frierson, D. M. W., I. M. Held, and P. Zurita-Gotor, 2006: A gray-radiation aquaplanet moist GCM. Part I: Static stability and eddy scale. *J. Atmos. Sci.*, **63**, 2548–2566, <https://doi.org/10.1175/JAS3753.1>.
- Guendelman, I., and Y. Kaspi, 2018: An axisymmetric limit for the width of the Hadley cell on planets with large obliquity and long seasonality. *Geophys. Res. Lett.*, **45**, 13 213–13 221, <https://doi.org/10.1029/2018GL080752>.
- , and —, 2019: Atmospheric dynamics on terrestrial planets: The seasonal response to changes in orbital, rotational, and radiative timescales. *Astrophys. J.*, **881**, 67, <https://doi.org/10.3847/1538-4357/ab2a06>.
- , and —, 2020: Atmospheric dynamics on terrestrial planets with eccentric orbits. *Astrophys. J.*, **901**, 46, <https://doi.org/10.3847/1538-4357/abae68>.
- Held, I. M., 2000: The general circulation of the atmosphere: 2000 program in geophysical fluid dynamics. WHOI Tech. Rep. WHOI-2001-03, 54 pp.
- , and A. Y. Hou, 1980: Nonlinear axially symmetric circulations in a nearly inviscid atmosphere. *J. Atmos. Sci.*, **37**, 515–533, [https://doi.org/10.1175/1520-0469\(1980\)037<0515:NASCIA>2.0.CO;2](https://doi.org/10.1175/1520-0469(1980)037<0515:NASCIA>2.0.CO;2).
- , and M. J. Suarez, 1994: A proposal for the intercomparison of the dynamical cores of atmospheric general circulation models. *Bull. Amer. Meteor. Soc.*, **75**, 1825–1830, [https://doi.org/10.1175/1520-0477\(1994\)075<1825:APFTIO>2.0.CO;2](https://doi.org/10.1175/1520-0477(1994)075<1825:APFTIO>2.0.CO;2).
- Hilgenbrink, C. C., and D. L. Hartmann, 2018: The response of Hadley circulation extent to an idealized representation of poleward ocean heat transport in an aquaplanet GCM. *J. Climate*, **31**, 9753–9770, <https://doi.org/10.1175/JCLI-D-18-0324.1>.
- Hill, S. A., 2021: Output of dry idealized GCM simulations under perpetual solstice-like forcing, version 1. Zenodo, accessed 21 December 2021, <https://doi.org/10.5281/ZENODO.5796233>.
- , S. Bordoni, and J. L. Mitchell, 2019: Axisymmetric constraints on cross-equatorial Hadley cell extent. *J. Atmos. Sci.*, **76**, 1547–1564, <https://doi.org/10.1175/JAS-D-18-0306.1>.
- , —, and —, 2020: Axisymmetric Hadley cell theory with a fixed tropopause temperature rather than height. *J. Atmos. Sci.*, **77**, 1279–1294, <https://doi.org/10.1175/JAS-D-19-0169.1>.
- , —, and —, 2021: Solstitial Hadley cell ascending edge theory from supercriticality. *J. Atmos. Sci.*, **78**, 1999–2011, <https://doi.org/10.1175/JAS-D-20-0341.1>.
- Hoskins, B. J., G.-Y. Yang, and R. M. Fonseca, 2020: The detailed dynamics of the June–August Hadley cell. *Quart. J. Roy. Meteor. Soc.*, **146**, 557–575, <https://doi.org/10.1002/qj.3702>.
- Kang, S. M., and J. Lu, 2012: Expansion of the Hadley cell under global warming: Winter versus summer. *J. Climate*, **25**, 8387–8393, <https://doi.org/10.1175/JCLI-D-12-00323.1>.
- Korty, R. L., and T. Schneider, 2008: Extent of Hadley circulations in dry atmospheres. *Geophys. Res. Lett.*, **35**, L23803, <https://doi.org/10.1029/2008GL035847>.
- Lee, H.-I., and J. L. Mitchell, 2021: The dynamics of quasi-stationary atmospheric rivers and their implications for monsoon onset. *J. Atmos. Sci.*, **78**, 2353–2365, <https://doi.org/10.1175/JAS-D-20-0262.1>.
- Levine, X. J., and T. Schneider, 2011: Response of the Hadley circulation to climate change in an aquaplanet GCM coupled to a simple representation of ocean heat transport. *J. Atmos. Sci.*, **68**, 769–783, <https://doi.org/10.1175/2010JAS3553.1>.
- , and —, 2015: Baroclinic eddies and the extent of the Hadley circulation: An idealized GCM study. *J. Atmos. Sci.*, **72**, 2744–2761, <https://doi.org/10.1175/JAS-D-14-0152.1>.
- Lindzen, R. S., and A. V. Hou, 1988: Hadley circulations for zonally averaged heating centered off the equator. *J. Atmos. Sci.*, **45**, 2416–2427, [https://doi.org/10.1175/1520-0469\(1988\)045<2416:HCFZAH>2.0.CO;2](https://doi.org/10.1175/1520-0469(1988)045<2416:HCFZAH>2.0.CO;2).
- Mitchell, J. L., and S. A. Hill, 2021: Constraints from invariant subtropical vertical velocities on the scalings of Hadley cell strength and downdraft width with rotation rate. *J. Atmos. Sci.*, **78**, 1445–1463, <https://doi.org/10.1175/JAS-D-20-0191.1>.
- , G. K. Vallis, and S. F. Potter, 2014: Effects of the seasonal cycle on superrotation in planetary atmospheres. *Astrophys. J.*, **787**, 23, <https://doi.org/10.1088/0004-637X/787/1/23>.
- O’Gorman, P. A., and T. Schneider, 2008: The hydrological cycle over a wide range of climates simulated with an idealized GCM. *J. Climate*, **21**, 3815–3832, <https://doi.org/10.1175/2007JCLI2065.1>.
- Plumb, R. A., and A. Y. Hou, 1992: The response of a zonally symmetric atmosphere to subtropical thermal forcing: Threshold behavior. *J. Atmos. Sci.*, **49**, 1790–1799, [https://doi.org/10.1175/1520-0469\(1992\)049<1790:TROAZS>2.0.CO;2](https://doi.org/10.1175/1520-0469(1992)049<1790:TROAZS>2.0.CO;2).
- Rodwell, M. J., and B. J. Hoskins, 1996: Monsoons and the dynamics of deserts. *Quart. J. Roy. Meteor. Soc.*, **122**, 1385–1404, <https://doi.org/10.1002/qj.49712253408>.
- Schneider, T., 2004: The tropopause and the thermal stratification in the extratropics of a dry atmosphere. *J. Atmos. Sci.*, **61**, 1317–1340, [https://doi.org/10.1175/1520-0469\(2004\)061<1317:TTATTS>2.0.CO;2](https://doi.org/10.1175/1520-0469(2004)061<1317:TTATTS>2.0.CO;2).

- , 2006: The general circulation of the atmosphere. *Annu. Rev. Earth Planet. Sci.*, **34**, 655–688, <https://doi.org/10.1146/annurev.earth.34.031405.125144>.
- , and S. Bordoni, 2008: Eddy-mediated regime transitions in the seasonal cycle of a Hadley circulation and implications for monsoon dynamics. *J. Atmos. Sci.*, **65**, 915–934, <https://doi.org/10.1175/2007JAS2415.1>.
- Singh, M. S., 2019: Limits on the extent of the solstitial Hadley cell: The role of planetary rotation. *J. Atmos. Sci.*, **76**, 1989–2004, <https://doi.org/10.1175/JAS-D-18-0341.1>.
- , 2021: Output of aquaplanet idealized GCM simulations under perpetual solstice-like forcing from Singh 2019, *J. Atmos. Sci.*, version 1. Zenodo, accessed 21 December 2021, <https://doi.org/10.5281/ZENODO.5796278>.
- Vallis, G. K., P. Zurita-Gotor, C. Cairns, and J. Kidston, 2015: Response of the large-scale structure of the atmosphere to global warming. *Quart. J. Roy. Meteor. Soc.*, **141**, 1479–1501, <https://doi.org/10.1002/qj.2456>.
- Walker, C. C., and T. Schneider, 2006: Eddy influences on Hadley circulations: Simulations with an idealized GCM. *J. Atmos. Sci.*, **63**, 3333–3350, <https://doi.org/10.1175/JAS3821.1>.
- Watt-Meyer, O., and D. M. W. Frierson, 2019: ITCZ width controls on Hadley cell extent and eddy-driven jet position and their response to warming. *J. Climate*, **32**, 1151–1166, <https://doi.org/10.1175/JCLI-D-18-0434.1>.
- Wei, H.-H., and S. Bordoni, 2018: Energetic constraints on the ITCZ position in idealized simulations with a seasonal cycle. *J. Adv. Model. Earth Syst.*, **10**, 1708–1725, <https://doi.org/10.1029/2018MS001313>.
- Zurita-Gotor, P., and I. M. Held, 2018: The finite-amplitude evolution of mixed Kelvin–Rossby wave instability and equatorial superrotation in a shallow-water model and an idealized GCM. *J. Atmos. Sci.*, **75**, 2299–2316, <https://doi.org/10.1175/JAS-D-17-0386.1>.